JGR Space Physics

RESEARCH ARTICLE
10.1029/2020JA028490

Conditions of Loss Cone Filling by Scattering on the Curved Field Lines for 30 keV Protons During Geomagnetic Storm as Inferred From Numerical Trajectory Tracing

S. Dubyagin[1], S. Apatenkov[2], E. Gordeev[2], N. Ganushkina[1,3], and Y. Zheng[4]

[1]Space and Earth Observation Centre, Finnish Meteorological Institute, Helsinki, Finland, [2]Earth's Physics Department, St. Petersburg State University, St. Petersburg, Russia, [3]Climate and Space Science and Engineering Department, University of Michigan, Ann Arbor, MI, USA, [4]Space Weather Laboratory, Code 674.0, NASA Goddard Space Flight Center, Greenbelt, MD, USA

Abstract The rate of pitch angle scattering on the curved magnetic field lines is well parameterized by the ratio of the minimum field line curvature radius to the maximum effective particle gyroradius ($K = R_C/r_g$). The critical value of this ratio (K_{cr}) corresponding to the loss cone filling is of special interest since it corresponds to the low altitude isotropic boundaries (IBs). The early theoretical estimates gave $K_{cr} = 8$, whereas recent estimations of the K parameter on the field lines corresponding to the observed IBs during the geomagnetic storms revealed K_{IB} values in the range of 3–30. We numerically trace the trajectories of the 30 keV protons in the magnetic field of the global magnetohydrodynamic simulation of the intense storm in order to infer statistical distribution of K_{cr}. The electric field and effects of nonstationarity are neglected in this study. It is found that although the K_{cr} values do show some variations during the course of the storm, its range is rather narrow $4 < K_{cr} < 8$. The result suggests that higher K_{IB} values found in the observational studies, if not caused by the magnetosphere-ionosphere mapping error, should be attributed to some other mechanism of pitch angle scattering. The K_{cr} values tend to be lower (4–6) during the main phase because the region of low K values approaches the Earth and the equatorial loss cone size becomes larger due to a larger equatorial magnetic field in the near-earth region. The remaining variation of K_{cr} is explained by the presence of the guide component of the magnetic field.

Key Points:

- 30 keV proton trajectories are traced to model the loss cone filling by scattering on the curved field lines during geomagnetic storm
- Critical value of adiabaticity parameter (K_{cr}) corresponding to the loss cone filling varies in the range of 4–8
- This K_{cr} variation is due to variations of the equatorial loss cone size and the guide component of magnetic field in the current sheet

Supporting Information:

- Supporting Information S1

Correspondence to:
S. Dubyagin,
stepan.dubyagin@fmi.fi

Citation:
Dubyagin, S., Apatenkov, S., Gordeev, E., Ganushkina, N., & Zheng, Y. (2021). Conditions of loss cone filling by scattering on the curved field lines for 30 keV protons during geomagnetic storm as inferred from numerical trajectory tracing. *Journal of Geophysical Research: Space Physics*, *126*, e2020JA028490. https://doi.org/10.1029/2020JA028490

Received 29 JUL 2020
Accepted 11 NOV 2020

1. Introduction

Two of the most debated processes violating the adiabatic ion motion in the nightside magnetosphere which lead to the particle scattering in the atmospheric loss cone are wave-particle interaction (e.g., Kennel & Petschek, 1966) and the scattering on the curved field lines in the magnetotail current sheet (e.g., Büchner & Zelenyi, 1989). Hereafter, the latter mechanism will be referred to as field line curvature (FLC) scattering. The ion interaction with waves mostly occurs in the inner magnetosphere (e.g., Erlandson & Ukhorskiy, 2001; Yahnin & Yahnina, 2007) whereas the FLC scattering is responsible for isotropic precipitations from the plasma sheet (Sergeev et al., 1993). Hypothetically, these two processes can operate collectively in the transition region between the plasma sheet and the inner magnetosphere and form merged precipitations.

In contrast to the pitch angle scattering due to wave-particle interaction, which depends on multiple parameters in a very complex manner, the amplitude of the FLC scattering is well parameterized by the adiabaticity (or curvature) parameter K: the ratio of the minimum curvature radius of the field line to the maximum effective particle gyroradius calculated for the full particle energy in the current sheet center (Büchner & Zeleny, 1986; Büchner & Zelenyi, 1989). The lower K, the stronger the scattering. Originally, the K parameter was defined for a simple symmetric magnetic field reversal configurations with zero guide component. In this study, we use the K definition generalized for arbitrary current sheet configurations as $K_{min} = \min(R_C/r_g)$, where the minimum is found along a given field line and curvature radius is calculated without any assumptions about the field line shape. It can be shown that the K_{min} parameter is roughly proportional to the squared magnetic field (Sergeev et al., 1993). For this reason, in the near-Earth region,

the K_{min} parameter increases sharply toward the Earth along with the magnetic field magnitude. At some critical point, the FLC scattering becomes too weak to deflect the particle in the atmospheric loss cone and this point corresponds to abrupt drop in the precipitating flux observed on the low-altitude satellites—so called isotropic boundary (IB).

Since the magnetic field in the equatorial magnetosphere undergoes dramatic variations with geomagnetic activity, the location of the inner boundary of the loss cone filling at the neutral sheet (and IB at low-altitude) also reveal the dynamic variations moving toward the Earth (equatorward) during the magnetic field depression and retreating tailward (poleward) during the recovery. For this reason, and because of availability and coverage of the low-altitude observations, isotropic boundaries (IBs) have been used for long time as a tool of the near-Earth magnetotail remote sensing (Sergeev et al., 1993; West et al., 1978), or as an index of geomagnetic activity (Asikainen et al., 2010; Gvozdevsky & Sergeev, 1996). In addition, analyses of the energetic proton trajectories in the test magnetic configurations were conducted by several authors to determine the critical value of the K_{min} parameter (K_{cr}) corresponding to the boundary where the scattering amplitude reaches the size of the loss cone and it becomes fully filled, and so that, corresponding to the IBs (Delcourt et al., 1996; Sergeev et al., 1983; Tsyganenko, 1982). For a several test analytical magnetic configurations, the narrow range of $K_{cr} = 6–10$ was found by the authors. This enables one to connect the low-altitude IB observations with characteristics of magnetic configuration of the magnetospheric empirical models and simulations and thus to assess their mapping accuracy (M. V. Kubyshkina et al., 1999; Shevchenko et al., 2010).

It should be stressed that all aforementioned IB applications are only possible if IB are formed by FLC scattering mechanism. However, the wave particle interaction also can lead to the isotropic precipitation and IB formation. For example, the localized isotropic precipitations of energetic protons equatorward from the typical IB location were indeed observed and their connection with electromagnetic ion cyclotron (EMIC) waves have been reliably established (Popova et al., 2018; Semenova et al., 2019; Yahnin & Yahnina, 2007). Gvozdevsky et al. (1997) studied the slightly anisotropic precipitation of energetic protons adjacent to IB (on equatorward side), apparently related to wave-particle interaction mechanism operating in the equatorial region. It can be speculated that strengthening of this mechanism would lead to IB formation at lower latitudes and mapped to the higher K_{min} region in the magnetotail. Finally, the condition $K_{cr} = const$ predicts that IBs for particles with different energies should reveal the energy dispersion with higher energy IBs located at lower latitudes (due to increase of a particle gyroradius with an energy increasing). However, the opposite dispersion is often observed (Donovan et al., 2003; Dubyagin et al., 2013; Sergeev et al., 2015) and can be explained by the wave-related mechanism of the IB formation (Liang et al., 2014). In contrast to FLC-scattering, the efficiency of the wave-induced scattering does not depend directly on K_{min} parameter and there is no reason to believe that this mechanism also produces IB at the $K_{min} = 6–10$ point.

One of the methods to elucidate the occurrences of the IBs formed by FLC and wave scattering is estimating the K_{min} at the field line corresponding to the observed IBs using empirical magnetospheric models or magnetohydrodynamic simulations. Hereinafter, we discriminate two notations: K_{cr} denotes a critical value of K_{min} corresponding to the loss cone filling by FLC-scattering obtained by numerical tracing of particle trajectories in the specific magnetic configurations (e.g., Sergeev et al., 1983), and K_{IB} denotes a value of K_{min} estimated at that field line where the real IB is observed, irrespective of the IB formation mechanism. The K_{IB} values which are close to the K_{cr} likely correspond to the FLC-scattering and K_{IB} values which are prominently greater than K_{cr} definitely correspond to some other mechanism of the pitch angle scattering.

Somewhat conflicting results were obtained for quiet-time IB observations: on one hand, Haiducek et al. (2019a) found that K_{IB} values for 30 keV protons were very close to K_{cr}; on the other hand, rather broad statistical distribution of the K_{IB} values ($K_{IB} \approx 3–30$) was found by Ilie et al. (2015) and Sergeev et al. (2015). The share of the high K_{IB} values is even higher during the geomagnetic storms; Dubyagin et al. (2018) and Haiducek et al. (2019b) reported that for ~20%–50% of storm time IBs the K_{IB} values were greater than 13. Such K_{IB} values apparently cannot be explained by FLC-scattering. These are not totally unexpected results because the occurrence of intense EMIC waves, which are capable of scattering the energetic protons into the loss cone, peaks during the geomagnetic storms (Chen et al., 2019; Halford et al., 2010; Keika et al., 2013; Usanova et al., 2012). On the other hand, the accuracy of the K_{IB} estimation is very difficult to assess and possibility that the broad distribution is a result of error in magnetosphere-ionosphere mapping or error of K_{min} estimation cannot be absolutely ruled out. In addition, the numerical values of K_{cr} were

obtained for a limited number of relatively simple analytical current sheet configurations: the parabolic and Harris current sheets as well as the current sheet of T89 magnetospheric model. At the same time, it was shown that there can be significant deviations from these K_{cr} values for more complex current sheet configurations (Delcourt et al., 2000, 2006). It is known that during a geomagnetic storm thin current sheet can develop at distances as close as $r \approx 5\ R_E$ or even closer (Tsyganenko & Sitnov, 2005, 2007). At this distance, the magnetic configuration at the IB formation region cannot be considered as one-dimensional and the near-Earth current can be bifurcated into horn-like configuration (Tsyganenko & Andreeva, 2017). For this reason, the range of K_{cr}-values obtained previously for the simple magnetic configurations might not be applicable for such configurations.

The purpose of this study is to statistically examine the condition of the loss cone filling by FLC scattering mechanism for a variety of current sheet configurations during intense geomagnetic storms. We performed numerical tracing of 30 keV proton trajectories in the magnetic field of MHD simulation of the intense storm event. The MHD representation of magnetic configuration is self-consistent with the isotropic plasma pressure and even if the actual configuration of the magnetosphere might be different, we expect that physics-based modeling results in a realistic configuration (Gordeev et al., 2015). The energy of 30 keV was chosen because it is covered by the majority of proton detectors on low-altitude satellites used for IB observations. 30 keV protons distributed over the loss cone were traced backward in time and their origin with respect to the loss cone in the opposite hemisphere was determined. Analyzing the percentage of the particles whose origins were outside the loss cone, we can determine the degree of loss cone filling. The particles were launched at different latitudes for seven MLT sectors covering the nightside during sudden commencement, main phase, early recovery phase with 1 h cadence. For each latitudinal profile, we determined the latitude where the loss cone became fully filled and calculated the K_{cr}-parameter on the corresponding field line. We present the statistical distribution of the K_{cr}-parameter and analyze the conditions in the field reversal region responsible for its variation. Possible effects related to the electric field or nonstationary magnetic configuration are ignored in this study.

2. MHD Simulation of the Storm June 22–26, 2015

The intense geomagnetic storms occurred on June 22–23, 2015 with the Dst index reaching minimum of −204 nT on 04 UT, June 23. There were three storm intensifications, but in this study we will focus only on the first two which occurred during 1.5 days interval June 22, 12 UT–June 24, 00 UT. Figure 1a shows the variation of the SYM-H index during this period (SYM-H and solar wind variations for the entire storm period can be found in M. Kubyshkina et al. (2019)).

The entire event was simulated by Space Weather Modeling Framework (SWMF) MHD model (Block Adaptive Tree Solar Wind-Roe-Upwind Scheme with Rice Convection Model [Tóth et al., 2005]) via the Community Coordinated Modeling Center's Runs-on-Request service with the running ID Yihua_Zheng_080416_2 run.

The near-Earth magnetosphere was well covered by the magnetic field observations on board six missions. M. Kubyshkina et al. (2019) compared these magnetic field observations to the SWMF output and found a remarkable agreement with the average error being within ∼20 nT with only ∼4 h period around 20 UT on June 22 when the error reached ∼60 nT; very good result for modeling such an intense storm. Though the error was large during the SYM-H drop at ∼20 UT on June 22, the agreement with observations for the particular moment is not critical for our study. Indeed, since the simulations obeys physical MHD equations, the SWMF configuration is expected to be realistic and physically consistent. The simulation spatial grid resolution is 0.25 R_E inside $|X|, |Y|, |Z| < 8\ R_E$ cube and 0.5 R_E outside that region. Since we are especially interested in the storm peak configurations when the thin current sheet approaches the Earth, we expect that the IB formation region will be inside the fine resolution region.

First, we use SWMF simulation to analyze how the distribution of the K-parameter changed during the course of the storm for different MLTs. For this purpose, the K-parameter for 30 keV protons was calculated on the meridional planes for seven nightside MLT sectors with 1 h temporal resolution. Since the MLT slices do not necessarily cross the simulation grid nodes, trilinear interpolation of the magnetic field vector components was used to calculate magnetic field between the grid nodes. The finite difference method was used

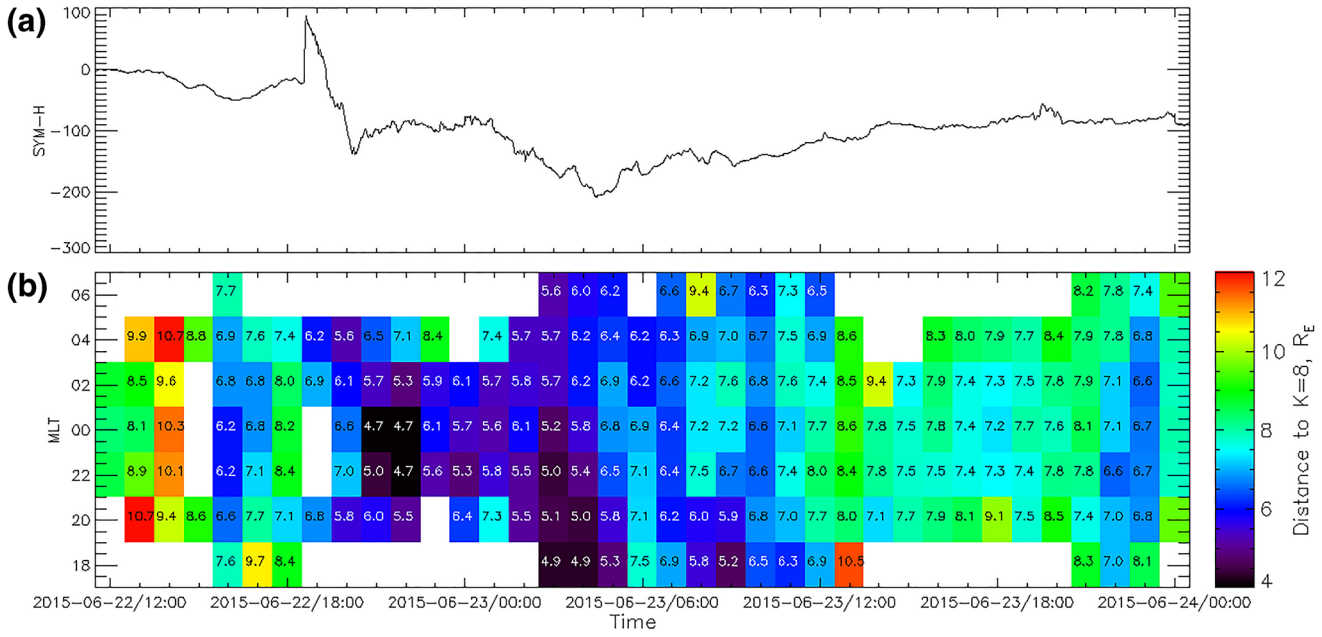

Figure 1. (a) Variation of the SYM-H index. (b) The radial distance to the earthward edge of the $K \leq 8$ region (color-coded in units of R_E) is shown as a function of time and MLT. The numbers inside the color bins duplicate the color indications.

for curvature radius estimation. Note also that although K was estimated on the meridional plane, it was calculated for the full 3D SWMF magnetic field and finite differences were calculated for all three directions. Since we are especially interested in the location of the region where IB is presumably formed, for every MLT slice, we find the earthward edge of $K \leq 8$ region. Figure 1b shows the result as time-MLT distribution. The radial distance to the closest (to the Earth) $K = 8$ point is color coded and also shown as a number in each time-MLT bin. It can be seen that the region with $K \leq 8$ comes to the Earth as close as $r = 4.7\ R_E$ during the main phase of the storm. There is also a moderate MLT asymmetry with low K region coming closer to the Earth at the dusk-midnight MLT sector. It can be also seen that some time-MLT bins are left blank. It is because we limited our search by $r = 12\ R_E$. Thus, the blank bins at 19 UT on June 22, during sudden commencement and following SYM-H drop, indicate that the $K \leq 8$ region moved outward ($r > 12\ R_E$) for MLT = 22–00 MLT sector. It can be interpreted as a localized depolarization. The thick current sheet also often forms at the flank MLT sectors and results in the blank bins at MLT = 18, MLT = 06.

For three time-MLT slices, we show the distribution of K-parameter in the meridional plane in Figure 2. Time and MLT are shown at the top of the figures. Three panels correspond to (a) prestorm period, (b) SYM-H minimum, and (c) early recovery phase. The blue region roughly corresponds to $K \leq 10$. It can be seen that in Figure 2b (corresponding to June 22, 22 UT, MLT = 22) this region is much thinner and located much closer to the Earth in comparison to Figures 2a and 2c. This can be considered as an indication of the thin intense current sheet formation but it should be remembered that there is no one-to-one correspondence between K and current density. Although this plot corresponds to the moment just after the SYM-H first minimum, it should be noted that the storm phase timing can be different in MHD simulation. Three white asterisks show the earthward edges of the regions of $K \leq 20$, $K \leq 8$, $K \leq 3$. Note that in Figure 2a, there are no $K \leq 3$ points inside $r = 12\ R_E$. Finally, it should be noted that the K estimate shown here is not very accurate due to trilinear interpolation of the field components and we use it as a first approximation.

3. Analytical Approximation of the Simulation Magnetic Field

To trace particle trajectories we need a physically consistent continuous and relatively smooth analytical approximation of the SWMF simulation magnetic field. It is convenient to use some magnetic potentials because this method provides divergence free magnetic field. We introduce additional simplification assuming

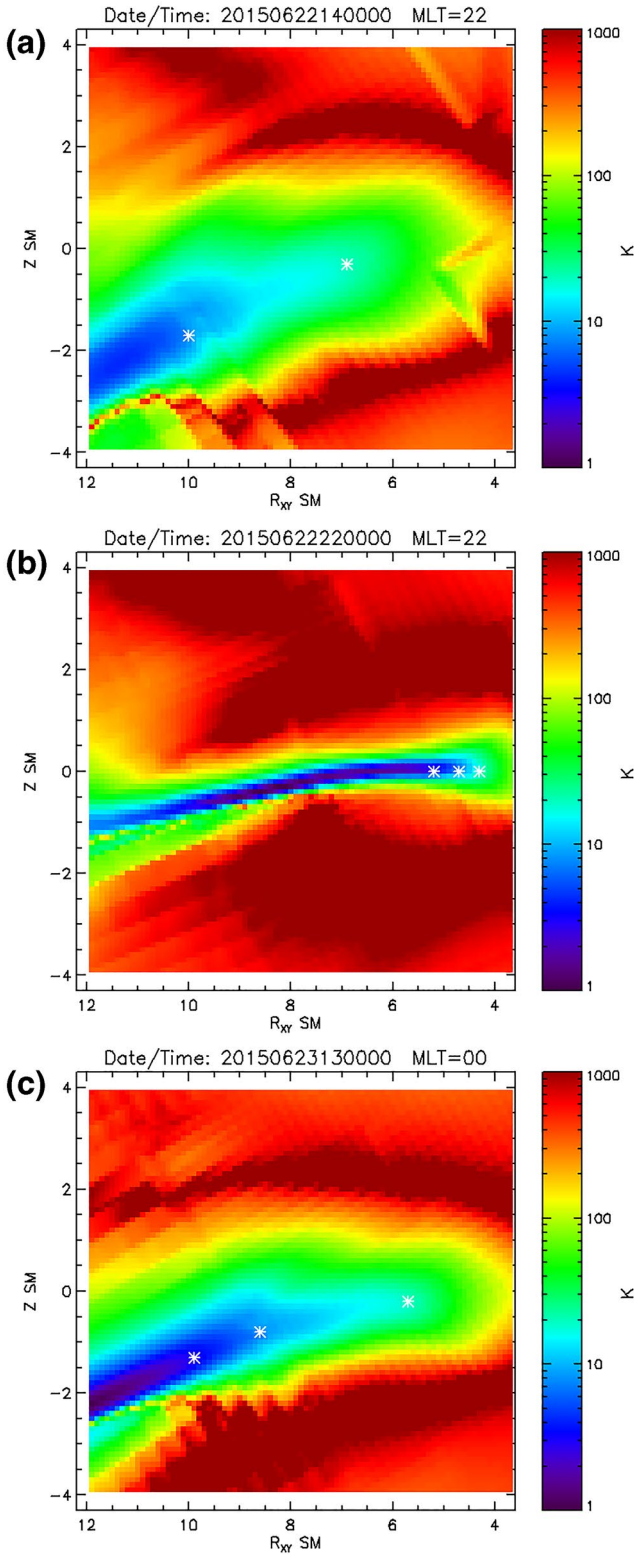

Figure 2. Examples of the *K*-parameter distribution in the meridional plane for (a) prestorm, (b) SYM-H minimum, and (c) early recovery phase.

that magnetic configuration possesses axial symmetry in SM coordinate system. We use Euler potentials (e.g., Stern, 1966) to describe magnetic field vector in meridional plane of SM system:

$$B = [\nabla\alpha \times \nabla\beta] \tag{1}$$

where α is a function of two cylindrical coordinates $\rho = (x^2 + y^2)^{\frac{1}{2}}$ and z, and $\beta = \varphi$ (azimuthal angle). In this case, for ρ and z components of magnetic field in cylindrical SM coordinates we get:

$$B_\rho = -\frac{1}{\rho}\frac{\partial\alpha}{\partial z} \tag{2}$$

$$B_z = \frac{1}{\rho}\frac{\partial\alpha}{\partial\rho} \tag{3}$$

Alpha is represented as a polynomial expansion:

$$\alpha(\rho,z) = \sum_{i=0}^{n}\sum_{j=0}^{m} C_{ij}\rho^i z^j \tag{4}$$

As a result, the field components depend on C_{ij} coefficients linearly and the magnetic field vectors can be fitted using usual least squares method.

Since for the axially symmetric configurations with $\partial B_\varphi/\partial\varphi = 0$ the magnetic field is divergence free for arbitrary $B_\varphi(\rho, z)$ distribution, there is no need to use any magnetic potential. We can use polynomial expansion directly for the B_φ component:

$$\alpha(\rho,z) = \sum_{i=0}^{n}\sum_{j=0}^{m} C_{ij}\rho^i z^j \tag{5}$$

Since we need the accurate magnetic field model only in the region where the particles undergo moderate pitch angle scattering, that is, K = 3–20, we developed automatic algorithm selecting the region on the meridional plane where the field is approximated. The example of this region selection can be seen in Figure 3a (shown by the blue curves). To select this region, we used the points shown as white asterisks in Figure 2 (these points correspond to K = 3, 8, 20 in the current sheet center). The outer boundary was located 1 R_E outward from the K = 3 point. For those events when there were no $K \le 3$ points inside r = 12 R_E, the outer boundary was set 2 R_E outward from the $K \le 8$ edge. In all cases, the outer boundary was set not further than r = 12 R_E. The inner boundary was set on a sphere with r = 3.3 R_E. The top and bottom boundaries were constructed as a combination of straight and dipole lines such that there was at least 0.5 R_E margin between the boundary and the field line corresponding to K = 3 point. Our analytic model (Equations 2–5) was fit to the SWMF magnetic field vectors on a meridional plane inside this region. It should be noted that Equations 2, 3 and 5 describe only external magnetic field of SWMF simulation with the dipole field subtracted. To give more weight to the points at low K region (low B regions), we minimized a mean relative error $Err = \Delta B/B$, where ΔB is a difference between the SWMF and the analytical model vectors, and B in the denominator is the full SWMF field magnitude (including dipole).

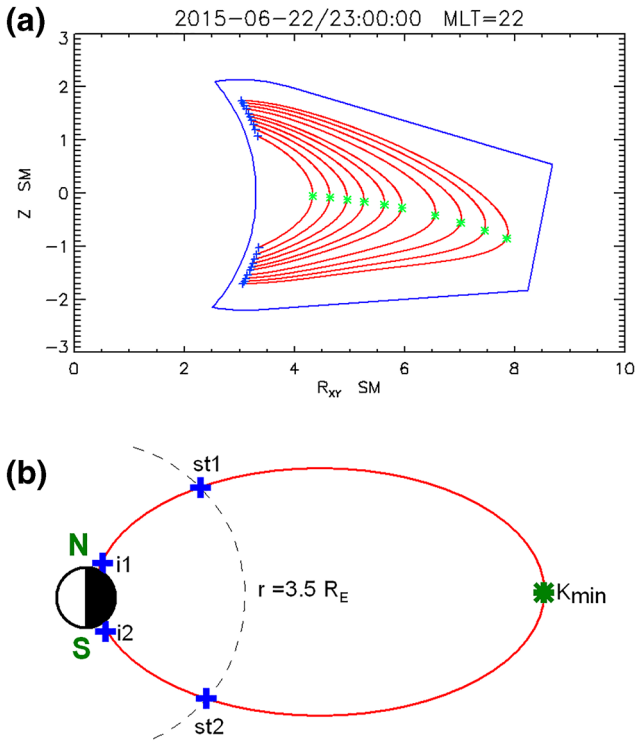

Figure 3. (a) Example of the field lines (red) traced from the starting points (blue crosses in the left part). The green asterisks near the field line apexes mark the location on K_{min}. Blue contour shows the boundary of the analytical approximation of the MHD simulation field. (b) The tracing configuration is explained.

To keep the number of terms in expansions for Euler potential and B_φ within reasonable limit and to avoid Runge's phenomenon (oscillation at the edges of an approximated interval that occurs when using polynomials of high degree), we elaborated the following strategy. First, we tried all combinations of the highest powers $1 \le n \le 8$ and $1 \le m \le 8$ and analyzed how the error of the approximations behaved. We plotted *Err* versus the total number of terms in these expansions ($N = n{\cdot}m$). It was noticed that *Err* for the Euler potential first decreased fast with N increasing but then it reached some level and did not reveal further significant decrease. On the contrary, the error for B_φ expansion revealed stable decrease with N increasing. It can be understood taking into account that we approximated 3D configuration by divergence free axially symmetric field. At some level of detalization, the divergence free approximation just cannot reproduce B_ρ and B_z distribution which is not divergence free because in 3D configuration zero divergence is ensured also by a variation in azimuthal direction ($\partial B_\varphi/\partial\varphi \neq 0$). To select the optimal values of n, m for the Euler potential fit, two reference values of the relative error are defined: Err_0 is the mean relative error when the SWMF magnetic field is approximated by its mean value, and Err_{min} is the minimum mean relative error over all possible combinations of $n < 8$ and $m < 8$. The optimal combination of n and m was defined in such a way that it gives minimum number of terms in the expansion and at the same time satisfies a condition $Err(n, m) \le Err_{min} + (Err_0 - Err_{min})/100$ (the error for the optimal n, m differs from Err_{min} less than 1% of difference between Err_0 and Err_{min}). For the B_φ fit, we used similar strategy for definition of optimal n, m but the requirement was simpler: minimal $N = n{\cdot}m$ for *Err* $(n, m) \le 0.01$. For the majority of configurations the n and m do not exceed value of 6. Two sets of the magnetic field expansion coefficients $C_{i,j}$, $A_{i,j}$, corresponding to the optimal n, m values for the Euler potential and B_φ approximations, were obtained for every time step and MLT sector. These coefficients represent the local axially symmetric analytical model-approximation of the SWMF field.

To assess the accuracy of out analytical model, we plot relative error of the SWMF magnetic field representation in Figure 4a (Figure 4c shows the obseved SYM-H index variation). The error is computed for the full field (external sources plus dipole) and shown versus time and MLT. The numbers duplicate the color representation. The median error is computed only for the region where the scattering take place $2 \le K \le 12$. It can be seen that the error is lowest during the main phase. It is due to smaller size of the region which should be modeled. Indeed, during the main phase $3 < K_{min} < 20$ region approaches the Earth (see the white points in Figure 2b), and the region where the field should be approximated becomes very small. On the other hand, the median errors can be as large as ~20% during the recovery phase. In Figure 4b, we show the relative error of the K parameter estimated from our analytical model. It generally reveals the variation similar to the magnetic field error but with somewhat larger values. Note that although the median relative error of 20% for some configurations seems to be very large, it usually corresponds to an absolute error $\Delta K \sim 1{-}2$ (see Figure S1 in supporting information).

4. Methodology

To model the loss cone filling as a function of K, we trace the trajectories of the particles with the initial velocity vectors inside the loss cone from a set of points above the ionosphere distributed in latitude and corresponding to different minimum K values at the magnetospheric part of the field line (K_{min}). To determine the correspondence between the latitudes and K_{min} values, the field lines should be traced from the starting points and K parameter should be calculated along the field lines. In addition, the size of the loss cone should be evaluated from the magnetic field magnitude at the opposite hemisphere. After the loss cone size is defined, the initial vectors of the particle velocities inside the loss cone can be set and the trajectory

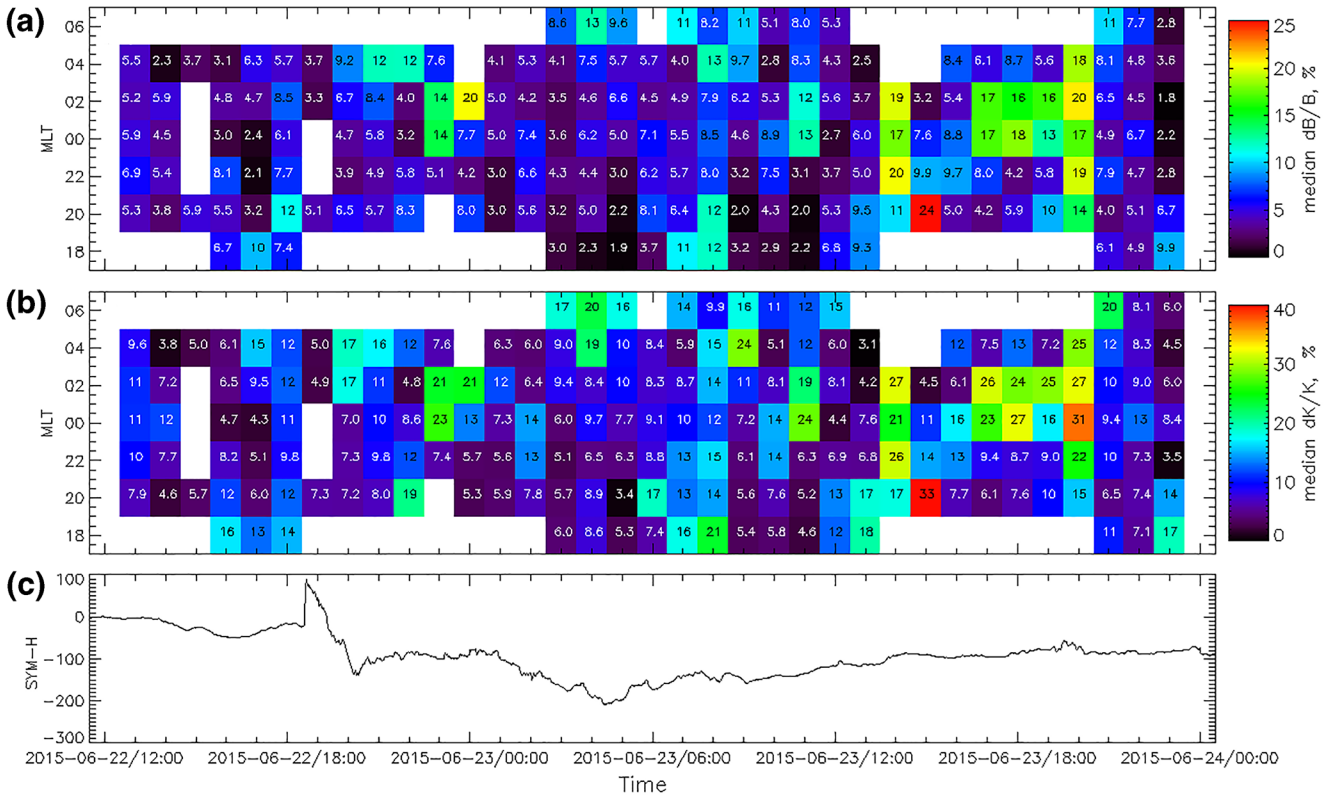

Figure 4. (a) The median relative error of the magnetic field analytic model. (b) The median relative error of the *K* parameter given by the analytic model. The errors are given in percents. (c) Variation of the SYM-H index.

tracing can be initiated. Thus, the sets of the spatial starting points with corresponding $K_{\min}$ values and the loss cone sizes should be defined for all desired MLT sectors and times.

4.1. Spatial Starting Points

One of the advantages of using Euler potential is simplicity and accuracy of the field line tracing because α is constant on a given field line. For every magnetic configuration, represented by its analytical model, we traced the magnetic field lines outward from the sphere $r = 3.5\ R_E$ (slightly above the inner boundary of the analytical model) via the equator and then to the sphere of the same radius in the opposite hemisphere. Figure 3b shows schematically the geometry. The field line is traced from the starting point in the northern hemisphere (st1) to the point in the southern hemisphere (st2). The *K*-parameter was calculated along the field line and a minimum value for a given field line was determined. Note, that in contrast to the *K*-parameter shown in Figures 1 and 2, which was calculated from the linearly interpolated SWMF magnetic field, this time the *K*-parameter is calculated using the smooth analytical model. Note that B_φ component was not ignored and also was used for the *K* calculation. The field line starting points were distributed in latitude to cover $3 \le K_{\min} \le 20$ region and the latitudinal increment was selected to keep the increment in $K_{\min}$ of ~1.

The loss cone size of the downgoing particles at the point st1 depends on the magnetic field magnitude in the opposite hemisphere at the altitude where the particles are lost due to collisions with the atmospheric particles (i2 point). Note that this loss cone definition differs from the traditional one which defines the loss cone size by the ionospheric magnetic field in the same hemisphere (i1 point). The altitude of the loss cone formation varies due to the atmosphere density variations but we use 120 km as a reference altitude of the loss cone formation in this study. Since our analytical model is defined only for the altitudes above $r = 3.5\ R_E$, we cannot use it for the field line tracing between st2 and i2 points. Instead, we trace the field lines between $r = 2.5 - 3.5\ R_E$ using trilinear interpolation of the MHD field, and below $r = 2.5\ R_E$, we use

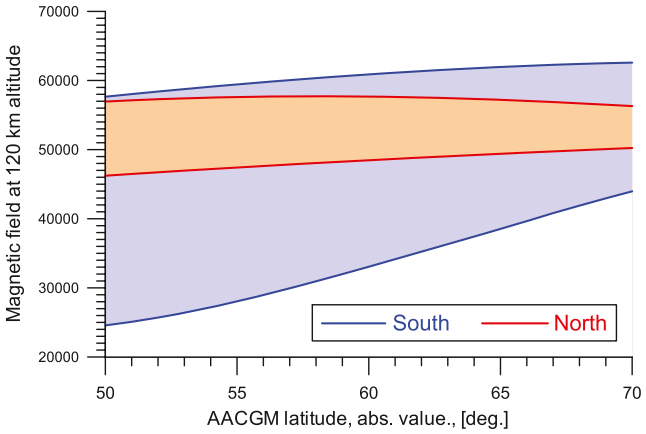

Figure 5. IGRF magnetic field at 120 km altitude versus absolute value of AACGM latitude. The filled areas between the red and blue curves show the span of the longitudinal variation for northern and southern hemispheres, respectively.

analytical equation for the dipole field line to project the points to the Earth's surface where a magnetic latitude of the point is calculated. Since the simulation uses a dipole representation of the Earth's field, this magnetic latitude can be interpreted as a Altitude-Adjusted Corrected Geomagnetic (AACGM) latitude.

The magnitude of the Earth's magnetic field at the ionospheric altitude depends both on the latitude and on the longitude. Figure 5 shows the magnitude of the IGRF model magnetic field at 120 km altitude versus AACGM latitude for two hemispheres. The upper and lower curves of the same color show the range of the longitudinal variation of the magnetic field for a given latitude. It can be seen that for the southern hemisphere, for the latitudes less than 60°, a longitudinal variation of the magnetic field can result in 2 times difference of the magnetic field magnitudes corresponding to the same AACGM latitude: manifestation of the South Atlantic Anomaly. Since the SWMF simulation lacks the longitudinal dependence of the Earth's field as well as to generalize our results to arbitrary longitudes and times, we use two extreme values of ionospheric magnetic field (upper and lower curves in Figure 5) for calculation of the loss cone size and the corresponding results will be designated by *Bi*_min and *Bi*_max suffixes.

We use the fifth-degree polynomial fits to the curves in Figure 5 to calculate the loss cone size for the AACGM latitude of the given magnetic field line. The analysis of the loss cone filling have been done for all four curves in Figure 5, but intermediate results are shown only for the loss cone size estimated from the minimum magnetic field magnitude in the southern hemisphere (lowest curve in Figure 5).

4.2. Initial Distribution in the Velocity Space

For a given kinetic energy ($E = 30$ keV is considered in this study), the magnetic moment corresponding to the loss cone edge (μ_{LC}) can be calculated as $\mu_{LC} = E/B_{i2}$. Thus, for the st1 point, the edge of the loss cone in the velocity space can be calculated as:

$$v_{\perp LC}^2 = \frac{2E}{m}\frac{B_{st1}}{B_{i2}} \tag{6}$$

After the loss cone size is determined, we set initial distributions of particle velocities in the velocity space: 372 points evenly distributed in $v_{\perp 1}$, $v_{\perp 2}$ plane inside the loss cone (see Figure 6). It should be noted that the magnetic moment conserves only in the frame moving with the guiding center (Stephens et al., 2017). The guiding center drift velocity is negligible at the ionospheric altitude but it cannot be neglected at $r = 3.5\ R_E$. For this reason, the velocity in the left part of Equation 6 is given for a drifting frame, and it should be converted to a stationary frame by addition of the drift velocity vector. The drift velocity vector was calculated using standard expressions for the gradient and curvature drifts (Baumjohann & Treumann, 1996) and finite difference for the magnetic field gradient and curvature radius estimation.

4.3. Numerical Methods and Accuracy Control

The particles were traced using fourth order Runge-Kutta-Nyström method (see e.g., Bock & Krischer, 1998). The method was used with a variable step-size computed for each new time-step as

$$\Delta t = \frac{\left(\Delta\alpha \cdot g\right)^{\frac{1}{4}}}{B}, \tag{7}$$

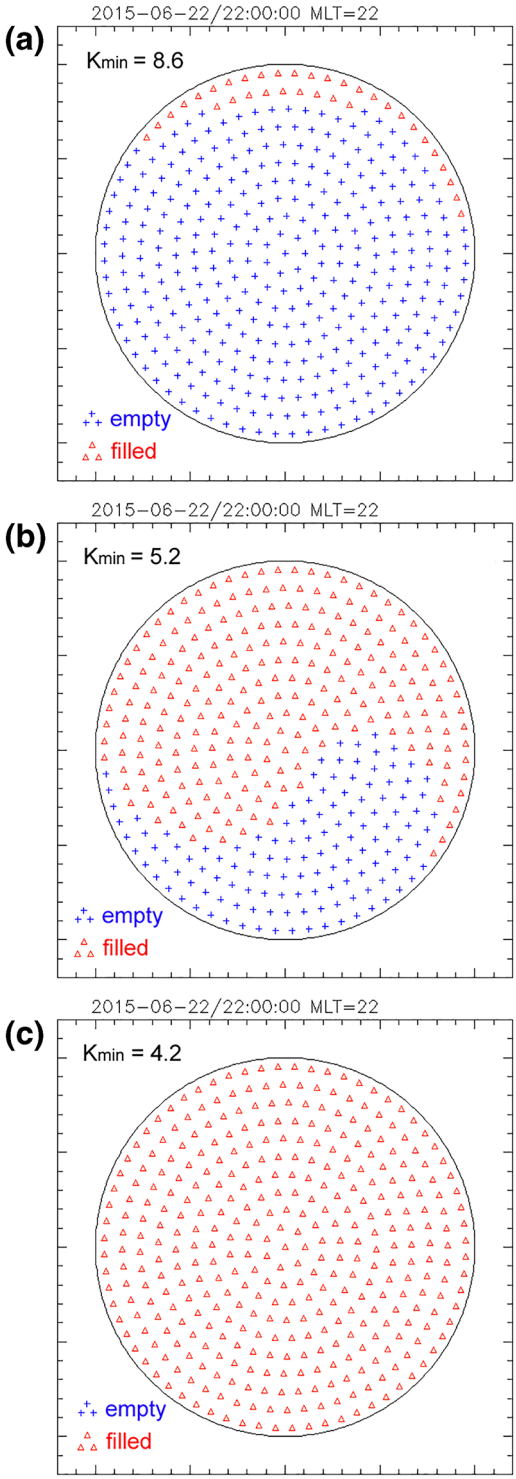

Figure 6. Distribution of the initial perpendicular velocities over the loss cone marked according to their origin outside (red) or inside (blue) of the opposite hemisphere loss cone. Three panels (a–c) correspond to three values of K_{min} (shown at the top left corner of the panel).

where B is the magnitude of magnetic field at the previous time-step, $\Delta\alpha$ is the allowed error in pitch angle at the ending point of a trajectory, and g is the constant calculated for each spatial starting point as described in supporting information S1 (the derivation of Equation 7 can be also found there). $\Delta\alpha$ is set to 1/200 of the loss cone size at the ending point. We have tested this step-size selection procedure performing backward in time and then forward in time tracings for several starting points and comparing initial and final pitch angles. For all tested trajectories the resulting error in pitch angle was at least 10 times smaller than the allowed error $\Delta\alpha$.

4.4. Trajectory Classification

For every time and MLT sector, we organize the tracing procedure as two embedded loops: one loop is over the spatial points (blue crosses at the left part of Figure 3a), and another one is for the velocity vectors inside the loss cone (evenly distributed points in Figure 6). There is a class of orbits for which the particle can be trapped near the current sheet for prolonged time (Kaufmann & Lu, 1993; Larson & Kaufmann, 1996; Speiser, 1965), for this reason we limit the time of tracing as double time needed for particle with zero pitch angle to reach the opposite hemisphere. Even at $r = 3.5\ R_E$, the loss cone size is still rather small (<10°), so the time required for the particle to reach the opposite hemisphere if no strong pitch angle scattering has occurred can be evaluated as L/v, where L is the length of the field line between st1 and st2 points (see Figure 3b), and v is the full particle velocity. Thus, the limit for the tracing time is $t_{\rm lim} = 2\ L/v$. Eventually, we trace the particle trajectories backward in time and tracing is stopped when one of the following conditions is met:

1. The particle reaches $r = 3.5\ R_E$ sphere in the opposite hemisphere
2. The particle returns back to $r = 3.5\ R_E$ in the same hemisphere (it is reflected from the minimum K region)
3. The particle crosses the outer boundaries of the magnetic field model applicability region (upper, lower, right blue lines in Figure 3a)
4. $t_{\rm lim} = 2\ L/v$ time is exceeded

For the vast majority of the trajectories, the first condition is met. In this case, the resulting particle velocity is converted to the drifting frame and the magnetic moment is calculated. The moment is compared to μ_{LC}, corresponding to the loss cone edge, to check whether the particle is still inside the loss cone or outside it. The latter result corresponds to the particle scattered into the loss cone during its crossing of the field reversal, while former results indicates that there is no particle at this point of the velocity space since there are no energetic particles going upward from the atmosphere. The conditions 2–4 correspond to the relatively strong pitch angle scattering, and although there is an uncertainty about the particle origin (because both options are possible after several crossing of the field reversal), these trajectories are marked as originated outside the loss cone.

5. Results

Figure 6 shows the initial distribution of the perpendicular velocities over the loss cone ($v_{\perp 1}$, $v_{\perp 2}$ normalized by perpendicular velocity corresponding to the loss cone edge) for the spatial points corresponding to

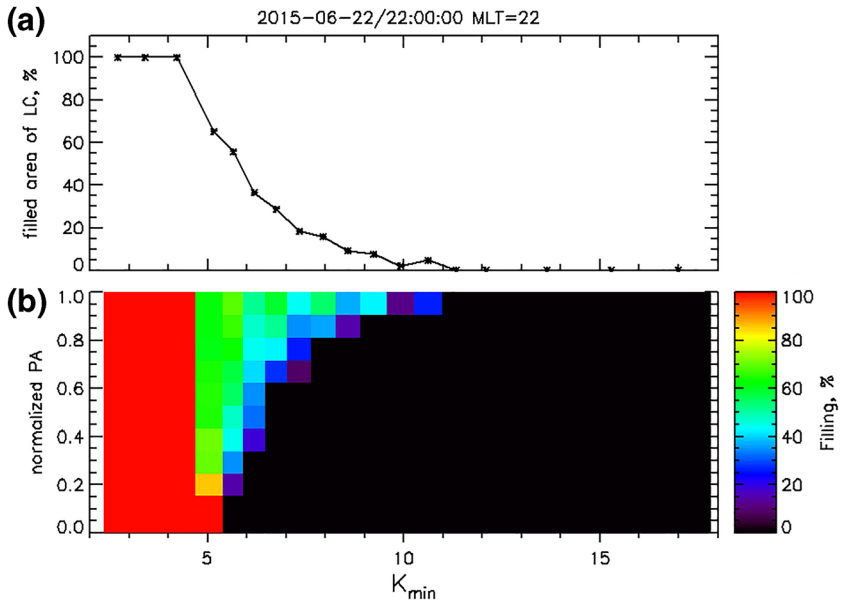

Figure 7. Diagrams showing the loss cone filling versus K_{min}-parameter. (a) Percentage of the loss cone area filled. (b) Color shows percentage of the loss cone filled for given pitch angle (normalized by loss cone size).

different K_{min} values (shown at the top of each panel). The blue crosses and red triangles correspond to the trajectories which are originated in the loss cone and outside the loss cone, respectively.

It can be seen that for $K_{min} = 8.6$ (Figure 6a), the scattering is weak and all trajectories originate in the loss cone. In reality, this would correspond to the empty loss cone. For lower K_{min} (Figure 6b), more than half of the loss cone is filled (the trajectories originate outside the loss cone, red triangles). Note, that the loss cone filling depends on the gyrophase. It is consistent with the Delcourt et al. (1995) results who showed that the amplitude of scattering depends on the gyration phase of the particle when it enters the low K region. It should be noted that this gyrophase dependence of the loss cone filling cannot be observed at low altitudes (e.g., 850 km; altitude of NOAA/POES satellites), because the difference in the number of gyrations for different pitch angles inside the loss cone becomes too large. Finally, at $K_{min} = 4.2$ (Figure 6c), whole loss cone is filled (all trajectories have their origins outside the loss cone).

Figure 7 demonstrates the process of the loss cone filling as a function of K_{min} at higher resolution. Figure 7a show the percentage of the loss cone area filled, calculated as a ratio of the velocity distribution points originated outside the loss cone to the total number of points. It can be seen that the loss cone filling starts at $K_{min} \approx 10$ and the loss cone becomes fully filled at $K_{min} = 4.2$. In Figure 7b, we show the process of the loss cone filling for different pitch angles. Since the points of velocity distribution in Figure 6 are organized in circles corresponding to certain pitch angle values, it is easy to calculate a percentage of the points originated outside the loss cone separately for each pitch angle. The vertical axis of Figure 7b shows the pitch angle normalized by the loss cone size (one corresponds to the loss cone edge). Color shows percentage of the loss cone area filled for the corresponding pitch angle. Red color corresponds to 100% filling. It can be seen that loss cone filling starts from its edge at $K_{min} \approx 10$, and gradually propagates to the center at $K_{min} \approx 5$.

Since the goal of this study is to explain the diversity of the K values estimated for the observed IBs, we need to develop a definition of an IB for the output of our trajectory computations, and this definition should be consistent with that for observations. Although the IBs can be observed even on high-altitude missions (Ganushkina et al., 2005), the most studies addressing this topic have been conducted using the observations of the NOAA/POES satellites at ~850 km altitude (Sergeev et al., 1993, 2015). These satellites are equipped with a suit of the solid state telescopes (Evans & Greer, 2004) pointing in the perpendicular directions one of which (referred to as 0° telescope) is directed radially upward and detects the fluxes of particles precipitating in the loss cone. Another one (referred to as 90° telescope), measures the fluxes of the locally trapped particles. At this altitude, the half-width of the loss cone varies between 45°–90°, and 30°-aperture of the NOAA/

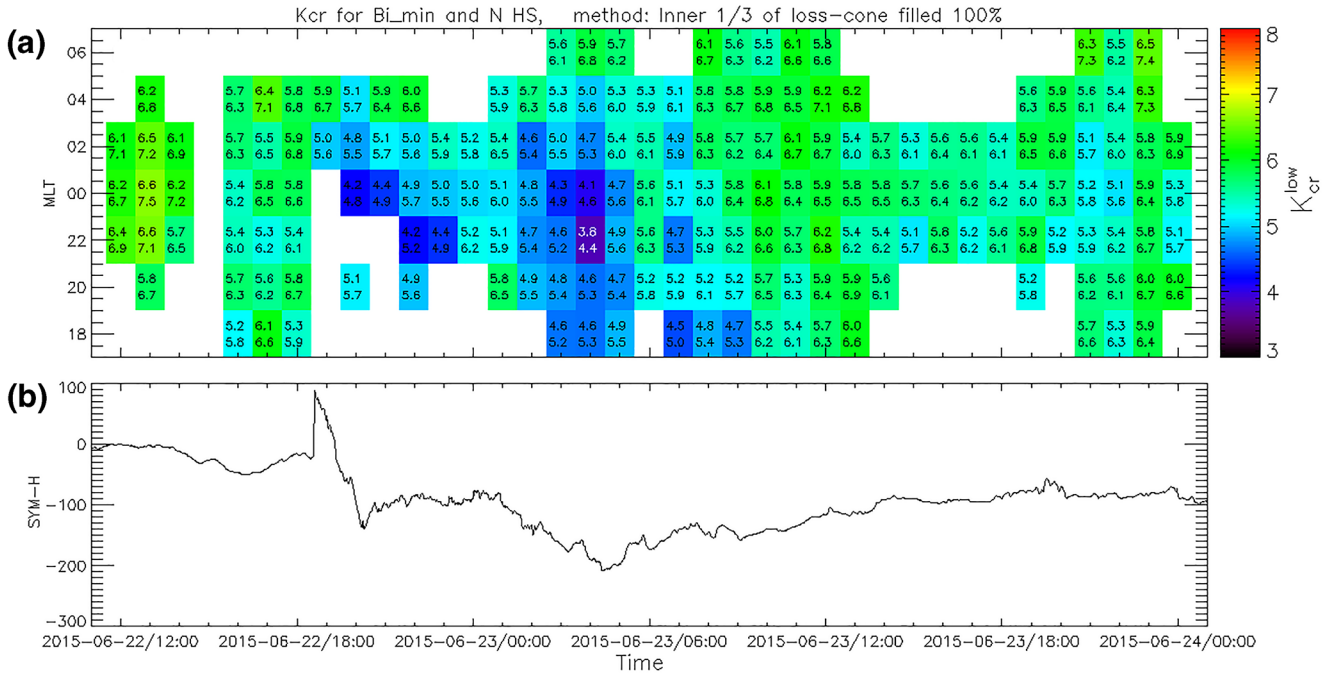

Figure 8. (a) The values of K_{cr}^{low} versus time and MLT are shown by color. The pairs of numbers overlapped over the plot show K_{cr}^{low} and K_{cr}^{up} for a given bin. (b) Variation of the SYM-H index.

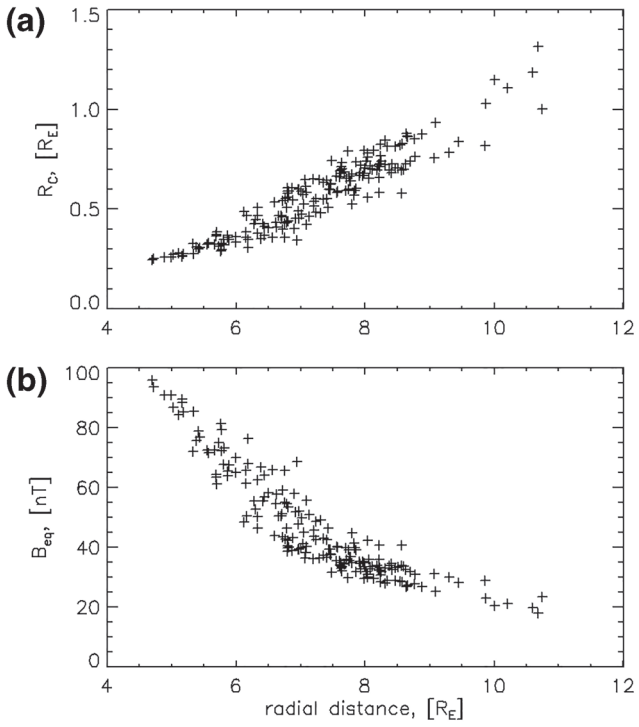

Figure 9. Parameters of the magnetic configuration at $K_{min} = 6$ point versus radial distance: (a) field line curvature radius, (b) magnetic field magnitude.

POES telescope fits reliably inside the loss cone. On the other hand, the telescope cannot see the outer part of the loss cone. In observations, the IB is defined as the most equatorial point where the fluxes are isotropic, that is, the fluxes detected by 0° and 90° telescopes are equal (within the accuracy of measurements). Therefore, we define the IB as a first point (moving from high to low K_{min} values) where the central 1/3 of the loss cone is 100% filled. This criterion typically corresponds to the filling of the more than 80% of the loss cone area (see Figure S2 in supporting information). However, since our discretization of the K_{min} values is rather coarse (the difference between the adjacent K_{min} values can be as large as ~1), we consider this K_{min} value as a lower estimate of the true K_{cr} and we also use the next higher K_{min} value as an upper estimate for K_{cr}. The corresponding K_{min} values are referred to as K_{cr}^{low} and K_{cr}^{up}, respectively.

Figure 8a shows the color-coded K_{cr}^{low} versus time and MLT. The pairs of numbers in the bins show K_{IB} and its upper estimate (next higher K_{min} value). It can be seen that K_{cr}^{low} does not exceed value of 7 and K_{cr}^{up} does not exceed value of 8. It can be noticed that somewhat more bins are left blank in comparison to Figure 1. This is because the algorithm cannot detect IB within the region of the magnetic field model validity; the values of K_{min} low enough to fill the loss cone are outside $r = 12R_E$. It should be noted that these configurations are not necessarily correspond to the depolarized current sheet. They often look as a plateau-like region at $K_{min} = 5$–6 level.

It is apparent from Figure 8 that there is a prominent variation of K_{cr} during the course of the storm: it is lower during the main phase of the storm especially at the premidnight sector where K_{cr}^{low} can be as low as

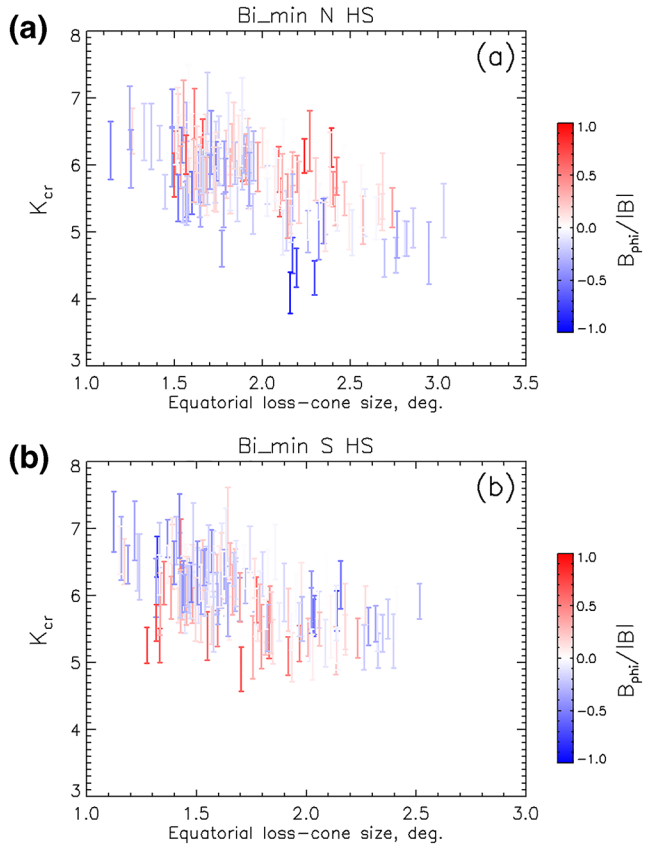

Figure 10. K_{cr} versus the loss cone size at the field reversal for the particles traced from (a) northern hemisphere, (b) southern hemisphere. The vertical error bars show the range between the K_{cr}^{low} and K_{cr}^{up}. Color corresponds to the normalized B_φ component.

~4. Note that it is roughly the same time and MLT sector when and where the region of the low K values approaches the Earth (see Figure 1b). This similarity is not just a coincidence. We analyzed the radial profiles of the $K_{\min}$ parameter and for each profile we identified the point where $K_{\min} = 6$. In Figure 9, we show the magnetic FLC radius (a) and equatorial magnetic field magnitude (b) at $K_{\min} = 6$ point versus radial distance. Each symbol corresponds to the individual $K_{\min}$ radial profile. It can be seen that the closer to the Earth the point $K_{\min} = 6$ is, the lower curvature radius corresponds to this $K_{\min}$ value. Since the gyroradius must follow the curvature radius to keep $K_{\min}$ constant and it depends inversely on magnetic field magnitude, the magnetic field is higher in the near-Earth region. In turn, higher equatorial magnetic field means larger loss cone size at the equator since it is expressed as $\alpha_{LC} = \arcsin\sqrt{B_{eq} / B_i}$ (here, B_i is magnetic field in the ionosphere). Hence, stronger scattering is needed to fill the larger loss cone and, therefore, the IB is formed at the lower $K_{\min}$ values in the near-Earth region during the main phase.

However, $K_{\min}$ is not the only parameter controlling the strength of the pitch angle scattering in the field reversal region. In Figure 10, we show K_{cr} versus the equatorial loss cone size. The vertical error bars show the range between lower and upper estimates of K_{cr}. Figures 10a and 10b correspond to the results obtained for particles traced from the northern and southern hemispheres, respectively. Although K_{cr} does display dependence on the loss cone size, the lowest values of K_{cr}^{low} are found for the mid-range values of the loss cone size. It was shown in a few studies that the guide-component of magnetic field at the field reversal region affects the intensity of the pitch angle scattering (Büchner & Zelenyi, 1991; Delcourt et al., 2000; Zhu & Parks, 1993). We use the color palette to shows the azimuthal component of the magnetic field (B_φ) normalized by the full magnetic field magnitude. It can be seen in Figure 10a that lowest K_{cr}^{low} values correspond to the strong negative B_φ, and more generally, bright blue and red error bars are located near the lower and upper envelopes of the data point cloud, respectively. The opposite dependence on B_φ can be seen in Figure 10b. Such interhemispheric asymmetry is in a full agreement with findings of Delcourt et al. (2000), who found that the pitch angle scattering strengthens or weakens depending on the mutual relationship between the directions of the particle propagation (and gyration) and the sign of the guide component at the field reversal. Note that the spread of the K_{cr} scatter due to B_φ variation is comparable to the range of variation caused by the variation of the loss cone size.

Figure 11 shows the histograms of K_{cr}^{low} (black) and iK_{cr}^{up} (red) for all times and MLT bins. Figures 11a and 11b are obtained using different models of the loss cone size dependence on AACGM latitude. The minimum value of the ionospheric magnetic field (lower blue curve in Figure 5) is used for Figure 11a and maximum value (upper blue curve in Figure 5) for Figure 11b. Since the loss cone size depends inversely on the ionospheric field magnitude, it is not surprising that the histograms in Figure 11b are shifted toward higher K_{cr} values. However, for both models of the ionospheric field, the values of K_{cr}^{low} does not exceed value of 7 and K_{cr}^{up} does not exceed value of 8. The peaks of the histograms are located between $K_{cr} = 6-7$. It is only a bit smaller than $K_{cr} = 8$ value, which is conventionally used in the studies where the IBs are analyzed (e.g., Shevchenko et al., 2010).

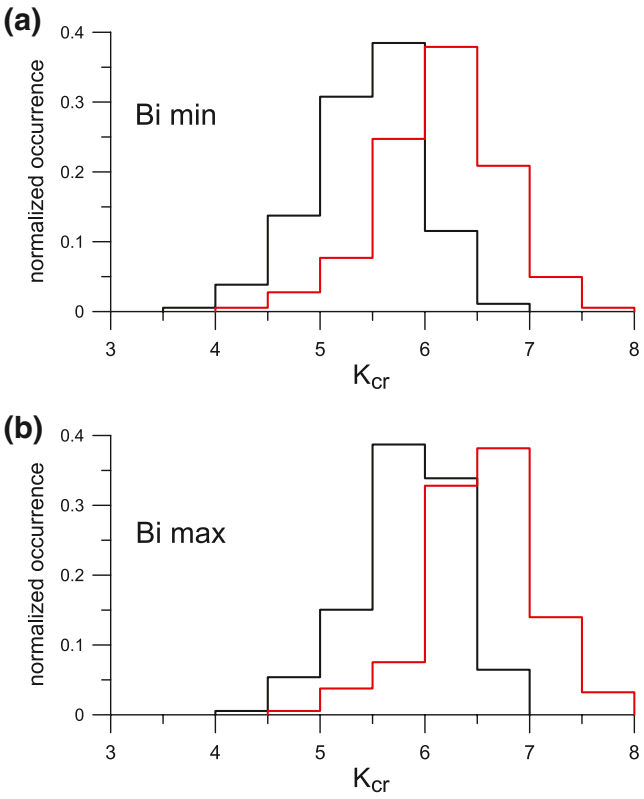

Figure 11. Histograms of K_{cr}^{low} (black) and K_{cr}^{up} (red). Panels (a and b) correspond to the results obtained using the minimum and maximum values of the ionospheric field, respectively. Particles were launched from the northern hemisphere.

6. Discussion

In this study, we modeled numerically the loss cone filling by 30 keV protons due to FLC scattering during the intense magnetospheric storm. The magnetic configuration was represented by the SWMF simulation. It was found that even the extreme configurations do not lead to significant changes of the loss cone filling conditions: the K_{cr} values do not exceed the value of 8. In fact, the K_{cr} values tend to be lower ($K_{cr} \approx 4$–6) during the main phase of the storm, when the $K_{min} < 8$ region can approach the Earth as close as $r \approx 5R_E$, and higher ($K_{cr} \approx 6$–8) during the prestorm interval and recovery. Although our results seem to indicate that all K_{IB} values greater than 8, found from the observations by Dubyagin et al. (2018) and Haiducek et al. (2019b), can be attributed to wave-particle interaction, yet, there is room for doubts. Our modeling has a number of serious limitations. The main limitation is that we fully neglect the electric field. The large scale electric field inside $L = 6$ can be as strong as 1.5–4 mV/m (e.g., Nishimura et al., 2006; Rowland & Wygant, 1998). Such field can significantly accelerate a proton even during single current sheet crossing. The analysis of the effects related to the electric field is left for the future study. On the practical side, it is conceivable that the periods with fast flows in the equatorial region manifest themselves specifically in the low-altitude observations and the corresponding IBs can be discarded or treated accordingly. This topic certainly deserves further investigation.

One more drawback of our approach is that we use axially symmetric local approximation of the SWMF field instead of 3D-interpolation between the simulation grid nodes. Figure 4a shows that the median error of our approximation can be as large as ~20%. In addition, the polynomial approximation with a moderate number of terms partly smooths the smallest-scale structures of the SWMF field. On the other hand, the advantage of our approach is that it provides divergence-free field which is fast to compute and the axially symmetric configuration simplifies the analysis (e.g., calculation of the guide field). At the very least, our approximation adequately describes the large-scale configuration in the near-Earth region with strong radial magnetic field gradient.

There are also a couple of minor effects which were also ignored. (1) An effect of the nonstationary configuration on the K_{cr} values is probably insignificant since it takes only 5 s for 30 keV proton to cross 2 R_E distance (estimate for field reversal region size) and less than 30 s to reach the ionosphere. (2) The K_{cr} values depend on the IB definition. All our results are obtained for IBs defined as the point where central one-third of the loss cone is 100% filled. We also tested a few other definitions and concluded that reasonable IB definitions do not lead to significant difference in K_{cr}.

On the other hand, there is still possibility that at least some fraction of IBs with large K_{IB} values found by Dubyagin et al. (2018) and Haiducek et al. (2019b) is accounted for by the errors of ionosphere-magnetosphere mapping and the K parameter estimation. It should be noted that in both studies, special efforts were undertaken to control the accuracy of the K estimation and mapping. The in situ magnetic field measurements in the region of expected IB formation were compared with the model magnetic field and the correction was applied taking into account the difference between the model and observations. However, the corrections were based on a number of assumptions, for example, linear dependence of estimated log K_{min} on B_Z error. It was also assumed that the magnetic field at the spacecraft location and at the point of true IB formation vary in a coherent manner (correlate with each other). In addition, Haiducek et al. (2019a) demonstrated that, apart from correction for the errors in equatorial B_Z, the correction of R_C is also needed, and this latter correction requires the probes located close enough to the current center (Liang et al., 2013). Such configurations are rather rare and were not available for the majority of IBs in Dubyagin et al. (2018) and Haiducek et al. (2019b) studies. At the same time, our Figure 9 demonstrates

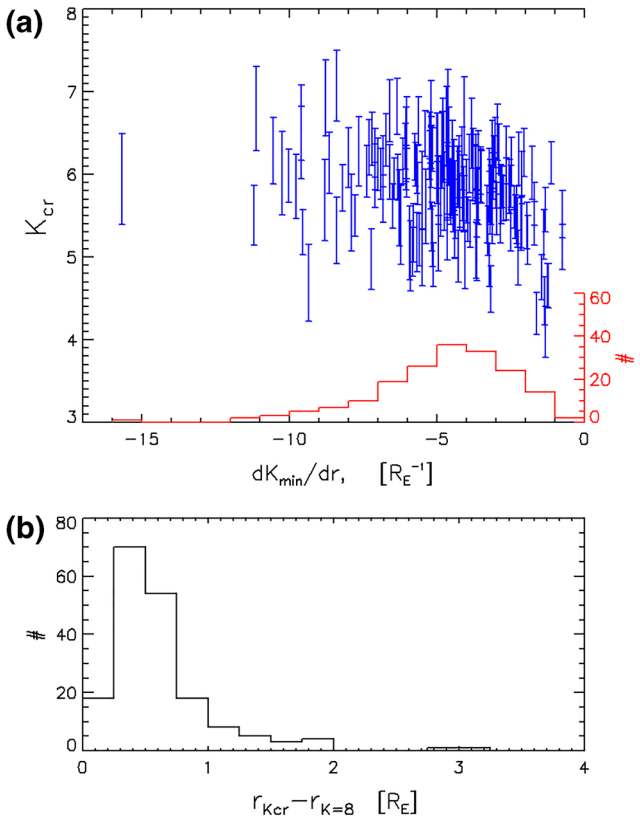

Figure 12. (a) K_{cr} versus K_{min} gradient (blue error bars) and histogram of K_{min} gradient (red bars). (b) Histogram of the difference between the radial distance to the true IB and the point with $K_{min} = 8$.

that the curvature radius in the IB vicinity undergoes strong variations during the course of the storm. This indicates that the R_C correction is more critical for the storm time than for the quiet period analyzed by Haiducek et al. (2019a).

In order to estimate the sensitivity of the K_{IB} estimation to the mapping error, we show K_{cr} versus the K_{min} radial gradient in Figure 12a. The blue error bars show the range between lower and upper estimates of K_{cr}. There is no clear dependence of K_{cr} on $\partial K_{min}/\partial r$. Note, however, that the three lowest K_{cr} values correspond to the weak gradient of $\sim -1 R_E^{-1}$. It is rather surprising because Figures 1 and 8 clearly demonstrate that the lowest K_{cr} values can be found during the peak of the storm in the near-Earth region where the radial gradients are supposed to be strong.

The histogram of K_{min} radial gradient is shown by red. It can be seen that for the majority of IBs, the absolute value of the gradient is in the range of 1–8 R_E^{-1} with the most probable value of ~4–5. Thus, if one assumes that the error of the mapping is 1 R_E, then the corresponding error of the K_{min} estimate is between 1 and 8. In other words, under such assumption, the mapping error can explain $K_{IB} \sim 15$, but it is unlikely that it will lead to higher values of K_{IB} estimates. Note that IBs with $K_{IB} > 15$ comprise a prominent share (~20%–30%) of the statistical distributions found in Dubyagin et al. (2018) and Haiducek et al. (2019b). On the other hand, the mapping error obviously depends on the configuration and is higher in the current sheet-like region. Therefore, the aforementioned arguments should be considered with caution. Note also, that Figure 9 shows that the loss cone filling occurs in higher B_{eq} region during the peak of the storm and this might partly compensate the mapping error related to worse performance of magnetic field models during these dynamic periods.

It can be clearly seen in Figure 8 that on the duskside the K_{cr} values are lower during the main phase and higher during the prestorm and recovery intervals. In Section 5, we have shown that it is due to larger size of the equatorial loss cone size at the IB location during the main phase. As a result, stronger scattering is required to fill the loss cone and the filling occurs at lower K_{cr} values. In turn, the larger loss cone size is due to larger equatorial magnetic field magnitude and this reflects specific properties of the main phase magnetic configuration: the same values of K_{min} correspond to the higher values of magnetic field magnitude and lower values of R_C.

We confirm the result of Delcourt et al. (2000) that the presence of the guide (azimuthal) component affects the strength of the pitch angle scattering and hence the K_{cr} values. It was found that the K_{cr} variation caused by B_φ in the SWMF simulation is comparable to that caused by the loss cone size variation. However, it should be noted that both effects, loss cone size and guide component variability, only cause K_{cr} variation within narrow range of $K_{cr} = 4$–8 and these values are rather close to those obtained previously for simpler magnetic configurations (Delcourt et al., 1996; Sergeev et al., 1983; Tsyganenko, 1982). Since K_{cr} values of 8 is conventionally used to tie the low-altitude IB observations to the equatorial magnetosphere (Shevchenko et al., 2010), we evaluate the size of the error in terms of equatorial radial distance which can result from using this fixed value instead of true K_{cr}. In Figure 12b, we show the histogram of the difference in radial distance to the points with $K_{min} = 8$ and $K_{min} = K_{cr}$. It can be seen that for most of the cases the error is within 1 R_E and only on rare occasions it can be as large as 2 or 3 R_E.

7. Summary

To analyze the conditions of the loss cone filling by the scattering on the curved field lines during intense geomagnetic storm, we traced the trajectories of 30 keV protons in the magnetic field of the SWMF simulation. The adiabaticity parameter (K_{cr}) corresponding to the boundary between the empty and filled loss cone was determined for several nightside MLT sectors throughout the course of the storm. The results are summarized as follows:

1. No K_{cr} values greater than 8 have been found indicating that the extreme storm time magnetic configuration alone (not considering the electric field and nonstationary effects) cannot cause the IB formation at the K_{cr} values greater than 8. The result suggests that higher K_{IB} values found in the observational studies for stationary periods, if not caused by the mapping error, should be attributed to the wave-particle interaction
2. The K_{cr} values tend to be lower (4–6) during the main phase and SYM-H minimum period
3. This variation of K_{cr} is caused partly by variation of the equatorial loss cone size: during the main phase, the K_{min} values typical for the IB correspond to much higher magnetic field, hence, stronger scattering is needed to fill the larger equatorial loss cone size and its filling occurs at lower K_{min} values
4. Another factor leading to variation of K_{cr} is the guide component of the magnetic field (B_φ). It affects the strength of the pitch angle scattering and hence K_{cr} values. The effect is comparable quantitatively to that related to the loss cone size variation

Data Availability Statement

Simulation results have been provided by the Community Coordinated Modeling Center at Goddard Space Flight Center through their public Runs on Request system (http://ccmc.gsfc.nasa.gov). The SWMF/BATS-R-US with RCM Model was developed by the Gombosi et al. at the Center for Space Environment Modeling, University of Michigan, USA, and Department of Physics and Astronomy, Rice University, Texas, USA.

Acknowledgments
The work leading to these results has been carried out in the Finnish Center of Excellence in Research of Sustainable Space (Academy of Finland grant numbers 312351, 312390), which we gratefully acknowledge. The collaboration between Finnish Meteorological Institute and St. Petersburg State University was supported by the Space Cooperation in the Science and Technology Commission between Finland and Russia (TT/AVA), Decision No 331895 of the Academy of Finland. Work of N. Ganushkina was supported by NASA grants #NNX17AI48G (ROSES 2016), #80NSSC20K0353 (ROSES 2018), and Heliophysics Phase I DRIVE Science Center SOLSTICE (Solar Storms and Terrestrial Impacts Center) #80NSSC20K0600. Work by E. Gordeev and S. Apatenko was supported by RFBR grant #19-05-00257.

References

Asikainen, T., Maliniemi, V., & Mursula, K. (2010). Modeling the contributions of ring, tail, and magnetopause currents to the corrected Dst index. *Journal of Geophysical Research*, *115*, A12203. https://doi.org/10.1029/2010JA015774

Baumjohann, W., & Treumann, R. (1996). *Basic space plasma physics*, 15–22. London, UK: Imperial College Press. https://doi.org/10.1142/p015

Bock, R. K., & Krischer, W. (1998). *The data analysis briefbook* (1st ed.). Berlin, Heidelberg: Springer-Verlag.

Büchner, J., & Zeleny, L. (1986). Deterministic chaos in the dynamics of charged particles near a magnetic field reversal. *Physics Letters A*, *118*(8), 395–399. https://doi.org/10.1016/0375-9601(86)90268-9

Büchner, J., & Zelenyi, L. M. (1989). Regular and chaotic charged particle motion in magnetotaillike field reversals: 1. Basic theory of trapped motion. *Journal of Geophysical Research*, *94*(A9), 11821–11842. https://doi.org/10.1029/JA094iA09p11821

Büchner, J., & Zelenyi, L. (1991). Regular and chaotic particle motion in sheared magnetic field reversals. *Advances in Space Research*, *11*(9), 177–182. https://doi.org/10.1016/0273-1177(91)90030-N

Chen, H., Gao, X., Lu, Q., & Wang, S. (2019). Analyzing EMIC waves in the inner magnetosphere using long-term Van Allen probes observations. *Journal of Geophysical Research: Space Physics*, *124*(9), 7402–7412. https://doi.org/10.1029/2019JA026965

Delcourt, D. C., Malova, H. V., & Zelenyi, L. M. (2006). Quasi-adiabaticity in bifurcated current sheets. *Geophysical Research Letters*, *33*, L06106. https://doi.org/10.1029/2005GL025463

Delcourt, D. C., Sauvaud, J. A., Martin, R. F., & Moore, T. E. (1995). Gyrophase effects in the centrifugal impulse model of particle motion in the magnetotail. *Journal of Geophysical Research*, *100*(A9), 17211–17220. https://doi.org/10.1029/95JA00657

Delcourt, D. C., Sauvaud, J.-A., Martin, R. F., & Moore, T. E. (1996). On the nondiabetic precipitation of ions from the near-Earth plasma sheet. *Journal of Geophysical Research*, *101*(A8), 17409–17418. https://doi.org/10.1029/96JA01006

Delcourt, D. C., Zelenyi, L. M., & Sauvaud, J.-A. (2000). Magnetic moment scattering in a field reversal with nonzero B_y component. *Journal of Geophysical Research*, *105*(A1), 349–359. https://doi.org/10.1029/1999JA900451

Donovan, E. F., Jackel, B., Klumpar, D., & Strangeway, R. (2003). Energy dependence of the isotropy boundary latitude. In *Proceedings of atmospheric studies by optical methods* (Vol. 92, pp. 11–14). Sodankylä Geophysical Observatory Publications.

Dubyagin, S., Ganushkina, N., Apatenkov, S., Kubyshkina, M., Singer, H., & Liemohn, M. (2013). Geometry of duskside equatorial current during magnetic storm main phase as deduced from magnetospheric and low-altitude observations. *Annales Geophysicae*, *31*(3), 395–408. https://doi.org/10.5194/angeo-31-395-2013

Dubyagin, S., Ganushkina, N. Y., & Sergeev, V. (2018). Formation of 30 keV proton isotropic boundaries during geomagnetic storms. *Journal of Geophysical Research: Space Physics*, *123*(5), 3436–3459. https://doi.org/10.1002/2017JA024587

Erlandson, R. E., & Ukhorskiy, A. J. (2001). Observations of electromagnetic ion cyclotron waves during geomagnetic storms: Wave occurrence and pitch angle scattering. *Journal of Geophysical Research*, *106*(A3), 3883–3895. https://doi.org/10.1029/2000JA000083

Evans, D., & Greer, M. (2004). Polar orbiting environmental satellite space environment monitor-2 instrument descriptions and archive data documentation. *NOAA Tech. Memo*, *1*, 4.

Ganushkina, N. Y., Pulkkinen, T. I., Kubyshkina, M. V., Sergeev, V. A., Lvova, E. A., Yahnina, T. A., et al. (2005). Proton isotropy boundaries as measured on mid- and low-altitude satellites. *Annales Geophysicae*, *23*, 1839–1847. https://doi.org/10.5194/angeo-23-1839-2005

Gordeev, E., Sergeev, V., Honkonen, I., Kuznetsova, M., Rastätter, L., Palmroth, M., et al. (2015). Assessing the performance of community-available global MHD models using key system parameters and empirical relationships. *Space Weather*, *13*(12), 868–884. https://doi.org/10.1002/2015SW001307

Gvozdevsky, B. B., & Sergeev, V. A. (1996). MT-index—A possible new index to characterize the configuration of the magnetotail. *Advances in Space Research*, *18*(8), 51–54. https://doi.org/10.1016/0273-1177(95)00995-7

Gvozdevsky, B. B., Sergeev, V. A., & Mursula, K. (1997). Long lasting energetic proton precipitation in the inner magnetosphere after substorms. *Journal of Geophysical Research*, *102*(A11), 24333–24338. https://doi.org/10.1029/97JA02062

Haiducek, J. D., Ganushkina, N. Y., Dubyagin, S., & Welling, D. T. (2019a). On the accuracy of adiabaticity parameter estimations using magnetospheric models. *Journal of Geophysical Research: Space Physics*, *124*(3), 1785–1805. https://doi.org/10.1029/2018JA025916

Haiducek, J. D., Ganushkina, N. Y., Dubyagin, S., & Welling, D. T. (2019b). The role of current sheet scattering in the proton isotropic boundary formation during geomagnetic storms. *Journal of Geophysical Research: Space Physics*, *124*(5), 3468–3486. https://doi.org/10.1029/2018JA026290

Halford, A. J., Fraser, B. J., & Morley, S. K. (2010). Emic wave activity during geomagnetic storm and nonstorm periods: CRRES results. *Journal of Geophysical Research*, *115*, A12248. https://doi.org/10.1029/2010JA015716

Ilie, R., Ganushkina, N., Toth, G., Dubyagin, S., & Liemohn, M. W. (2015). Testing the magnetotail configuration based on observations of low-altitude isotropic boundaries during quiet times. *Journal of Geophysical Research: Space Physics*, *120*(12), 10557–10573. https://doi.org/10.1002/2015JA021858

Kaufmann, R. L., & Lu, C. (1993). Cross-tail current: Resonant orbits. *Journal of Geophysical Research*, *98*(A9), 15447–15465. https://doi.org/10.1029/93JA01464

Keika, K., Takahashi, K., Ukhorskiy, A. Y., & Miyoshi, Y. (2013). Global characteristics of electromagnetic ion cyclotron waves: Occurrence rate and its storm dependence. *Journal of Geophysical Research: Space Physics*, *118*(7), 4135–4150. https://doi.org/10.1002/jgra.50385

Kennel, C. F., & Petschek, H. E. (1966). Limit on stably trapped particle fluxes. *Journal of Geophysical Research*, *71*(1), 1–28. https://doi.org/10.1029/JZ071i001p00001

Kubyshkina, M. V., Sergeev, V. A., & Pulkkinen, T. I. (1999). Hybrid input algorithm: An event-oriented magnetospheric model. *Journal of Geophysical Research*, *104*(A11), 24977–24993. https://doi.org/10.1029/1999JA900222

Kubyshkina, M., Sergeev, V. A., Tsyganenko, N. A., & Zheng, Y. (2019). Testing efficiency of empirical, adaptive, and global MHD magnetospheric models to represent the geomagnetic field in a variety of conditions. *Space Weather*, *17*(5), 672–686. https://doi.org/10.1029/2019SW002157

Larson, D. J., & Kaufmann, R. L. (1996). Structure of the magnetotail current sheet. *Journal of Geophysical Research*, *101*(A10), 21447–21461. https://doi.org/10.1029/96JA01945

Liang, J., Donovan, E., Ni, B., Yue, C., Jiang, F., & Angelopoulos, V. (2014). On an energy-latitude dispersion pattern of ion precipitation potentially associated with magnetospheric EMIC waves. *Journal of Geophysical Research: Space Physics*, *119*(10), 8137–8160. https://doi.org/10.1002/2014JA020226

Liang, J., Donovan, E., Spanswick, E., & Angelopoulos, V. (2013). Multiprobe estimation of field line curvature radius in the equatorial magnetosphere and the use of proton precipitations in magnetosphere-ionosphere mapping. *Journal of Geophysical Research: Space Physics*, *118*(8), 4924–4945. https://doi.org/10.1002/jgra.50454

Nishimura, Y., Shinbori, A., Ono, T., Iizima, M., & Kumamoto, A. (2006). Storm-time electric field distribution in the inner magnetosphere. *Geophysical Research Letters*, *33*, L22102. https://doi.org/10.1029/2006GL027510

Popova, T. A., Yahnin, A. G., Demekhov, A. G., & Chernyaeva, S. A. (2018). Generation of EMIC waves in the magnetosphere and precipitation of energetic protons: Comparison of the data from THEMIS high Earth orbiting satellites and POES low Earth orbiting satellites. *Geomagnetism and Aeronomy*, *58*(4), 469–482. https://doi.org/10.1134/S0016793218040114

Rowland, D. E., & Wygant, J. R. (1998). Dependence of the large-scale, inner magnetospheric electric field on geomagnetic activity. *Journal of Geophysical Research*, *103*(A7), 14959–14964. https://doi.org/10.1029/97JA03524

Semenova, N. V., Yahnin, A. G., Yahnina, T. A., & Demekhov, A. G. (2019). Properties of localized precipitation of energetic protons equatorward of the isotropic boundary. *Geophysical Research Letters*, *46*(20), 10932–10940. https://doi.org/10.1029/2019GL085373

Sergeev, V. A., Chernyaev, I. A., Angelopoulos, V., & Ganushkina, N. Y. (2015). Magnetospheric conditions near the equatorial footpoints of proton isotropy boundaries. *Annales Geophysicae*, *33*(12), 1485–1493. https://doi.org/10.5194/angeo-33-1485-2015

Sergeev, V. A., Chernyaeva, S. A., Apatenkov, S. V., Ganushkina, N. Y., & Dubyagin, S. V. (2015). Energy-latitude dispersion patterns near the isotropy boundaries of energetic protons. *Annales Geophysicae*, *33*(8), 1059–1070. https://doi.org/10.5194/angeo-33-1059-2015

Sergeev, V. A., Malkov, M., & Mursula, K. (1993). Testing the isotropic boundary algorithm method to evaluate the magnetic field configuration in the tail. *Journal of Geophysical Research*, *98*(A5), 7609–7620. https://doi.org/10.1029/92JA02587

Sergeev, V. A., Sazhina, E. M., Tsyganenko, N. A., Lundblad, J. A., & Soraas, F. (1983). Pitch-angle scattering of energetic protons in the magnetotail current sheet as the dominant source of their isotropic precipitation into the nightside ionosphere. *Planetary and Space Science*, *31*(10), 1147–1155. https://doi.org/10.1016/0032-0633(83)90103-4

Shevchenko, I. G., Sergeev, V., Kubyshkina, M., Angelopoulos, V., Glassmeier, K. H., & Singer, H. J. (2010). Estimation of magnetosphere-ionosphere mapping accuracy using isotropy boundary and THEMIS observations. *Journal of Geophysical Research*, *115*, A11206. https://doi.org/10.1029/2010JA015354

Speiser, T. W. (1965). Particle trajectories in model current sheets: 1. Analytical solutions. *Journal of Geophysical Research*, *70*(17), 4219–4226. https://doi.org/10.1029/JZ070i017p04219

Stephens, C. D., Brzozowski, R. W., & Jenko, F. (2017). On the limitations of gyrokinetics: Magnetic moment conservation. *Physics of Plasmas*, *24*(10), 102517. https://doi.org/10.1063/1.4998968

Stern, D. P. (1966). The motion of magnetic field lines. *Space Science Reviews*, *6*(2), 147–173. https://doi.org/10.1007/BF00222592

Tóth, G., Sokolov, I. V., Gombosi, T. I., Chesney, D. R., Clauer, C. R., De Zeeuw, D. L., et al. (2005). Space Weather Modeling Framework: A new tool for the space science community. *Journal of Geophysical Research*, *110*, A12226. https://doi.org/10.1029/2005JA011126

Tsyganenko, N. A. (1982). Pitch-angle scattering of energetic particles in the current sheet of the magnetospheric tail and stationary distribution functions. *Planetary and Space Science*, *30*(5), 433–437. https://doi.org/10.1016/0032-0633(82)90052-6

Tsyganenko, N. A., & Andreeva, V. A. (2017). A hybrid approach to empirical magnetosphere modeling. *Journal of Geophysical Research: Space Physics*, *122*(8), 8198–8213. https://doi.org/10.1002/2017JA024359

Tsyganenko, N. A., & Sitnov, M. I. (2005). Modeling the dynamics of the inner magnetosphere during strong geomagnetic storms. *Journal of Geophysical Research*, *110*, A03208. https://doi.org/10.1029/2004JA010798

Tsyganenko, N. A., & Sitnov, M. I. (2007). Magnetospheric configurations from a high-resolution data-based magnetic field model. *Journal of Geophysical Research*, *112*, A06225. https://doi.org/10.1029/2007JA012260

Usanova, M. E., Mann, I. R., Bortnik, J., Shao, L., & Angelopoulos, V. (2012). THEMIS observations of electromagnetic ion cyclotron wave occurrence: Dependence on AE, SYMH, and solar wind dynamic pressure. *Journal of Geophysical Research: Space Physics*, *117*, A10218. https://doi.org/10.1029/2012JA018049

West, H. I., Buck, R. M., & Kivelson, M. G. (1978). On the configuration of the magnetotail near midnight during quiet and weakly disturbed periods: Magnetic field modeling. *Journal of Geophysical Research*, *83*(A8), 3819–3829. https://doi.org/10.1029/JA083iA08p03819

Yahnin, A., & Yahnina, T. (2007). Energetic proton precipitation related to ion-cyclotron waves. *Journal of Atmospheric and Solar-Terrestrial Physics*, *69*(14), 1690–1706. https://doi.org/10.1016/j.jastp.2007.02.010

Zhu, Z., & Parks, G. (1993). Particle orbits in model current sheets with a nonzero B_y component. *Journal of Geophysical Research*, *98*(A5), 7603–7608. https://doi.org/10.1029/92JA02366